Synthesis and characterization of kaolinite-supported zero-valent iron nanoparticles and their application for the removal of aqueous Cu2+ and Co2+ ions

6 authors, including:

Cagri Üzüm
Surflay Nanotec GmbH
14 PUBLICATIONS   540 CITATIONS

SEE PROFILE

Talal Shahwan
Birzeit University
54 PUBLICATIONS   1,293 CITATIONS

SEE PROFILE

Keith Richard Hallam
University of Bristol
89 PUBLICATIONS   1,604 CITATIONS

SEE PROFILE

Thomas Bligh Scott
University of Bristol
83 PUBLICATIONS   1,836 CITATIONS

SEE PROFILE

Synthesis and characterization of kaolinite-supported zero-valent iron nanoparticles and their application for the removal of aqueous Cu^{2+} and Co^{2+} ions

Ç. Üzüm [a], T. Shahwan [a,*], A.E. Eroğlu [a], K.R. Hallam [b], T.B. Scott [b], I. Lieberwirth [c]

[a] Department of Chemistry, Izmir Institute of Technology, Urla 35430, Izmir, Turkey
[b] Interface Analysis Centre, University of Bristol, 121 St Michael's Hill, Bristol BS2 8BS, United Kingdom
[c] Max Planck Institute for Polymer Research, Ackermannweg 10, 55128 Mainz, Germany

ARTICLE INFO

ABSTRACT

This study reports the synthesis and characterization of nano-scale zero-valent iron in the presence of kaolinite clay (nZVI-kaol). The adsorbent, nZVI-kaol, was produced at initial Fe:kaolinite mass ratios of 1:1, 0.5:1, and 0.2:1. The presence of kaolinite resulted in decreased aggregation of iron nanoparticles, yielding composites with iso-electric points (IEPs) around 6.7–7.0. The reduction in Fe^{2+} precursor concentration appeared to decrease further the extent of aggregation and the size of individual nZVI particles. The synthesized nZVI-kaol materials were then tested for the removal of aqueous Cu^{2+} and Co^{2+} ions. The investigated parameters in the uptake experiments included volume/mass (V/M) ratio, initial concentrations of Cu^{2+} and Co^{2+} ions, contact time, pH, and repetitive application of the adsorbent. The adsorbents demonstrated high removal abilities towards both cations under the investigated conditions. Repetitive loading tests showed that significant removal could still be achieved at small concentrations by samples reused several times. X-ray photoelectron spectroscopy (XPS) analysis showed that while Co^{2+} was mainly fixed by the oxyhydroxyl groups of iron nanoparticles, Cu^{2+} ions were fixed by a redox mechanism, leading to the formation of Cu$_2$O and Cu^0.

1. Introduction

Iron particles with nano-scale size have been recently reported to demonstrate excellent uptake capabilities toward various types of metallic ions (Ponder et al., 2000; Kanel et al., 2005, 2006; Li and Zhang, 2006, 2007; Çelebi et al., 2007; Macdonald et al., 2007; Karabelli et al., 2008; Üzüm et al., in press). Although there are some uncertainties regarding the fundamental features of iron nanotechnology, the application of iron nanoparticles is considered as a rapidly emerging prominent technology with considerable potential benefits (Tratnyek and Johnson, 2006). Zero valent iron (ZVI) in powder or granular form has been applied as a reactive material in permeable reactive barriers (PRBs) for the removal of different pollutants (Baird, 1999; Blowes et al., 2000). The application of ZVI in nano-size can improve the reactivity of the material by virtue of the high surface to volume ratio and could also bring about kinetic advantages for adsorption (Huber, 2005). Another important property of these nanoparticles is their enormous flexibility for in situ and ex situ applications (Zhang, 2003).

Modified iron nanoparticles have been synthesized in order to enhance the speed and efficiency of remediation (Zhang, 2003). When the reduction of an aqueous iron salt is done in the presence of a support material, the normally-observed aggregation of iron nanoparticles was reported to decrease (Ponder et al., 2000; Zhang et al., 2006). The resulting dispersion of iron nanoparticles offers a higher specific surface area and consequently a higher reactivity of iron to the aqueous stream.

Adequate delivery of nZVI in soil and groundwater bodies is identified as an important difficulty in the application of this technology for in situ remediation (Li et al., 2006). Synthesizing nZVI on minerals that can fit into the geochemical conditions might offer one of the solutions to overcome the aforementioned problem. To our knowledge, no report is yet available in the literature on the application of clay minerals for this purpose. In this study, kaolinite was tested as a support material for iron nanoparticles. Kaolinite is known for its structural stability within geochemical conditions, ability to act as adsorbent and wide availability across the geomedia. By virtue of these properties, clays could be suitable for hosting nZVI in permeable reactive barriers or remediation systems.

Cobalt is among the elements encountered in industrial wastes. The radioisotope ^{60}Co ($t_{1/2}$ = 5.3 y) is extensively used in medicine for cancer treatment as well as for sterilization purposes. Copper is also among the most common pollutants in industrial effluents. This element is an essential trace element for living organisms, but its intake at high levels can cause detrimental health effects.

The objective of this work in its first part was to synthesize and characterize nZVI in the presence of kaolinite at three different nZVI: kaolinite ratios. In the second part, two of the samples (those containing highest and lowest Fe contents) were tried as adsorbents of aqueous Co^{2+} and Cu^{2+} ions. The experiments were performed under a
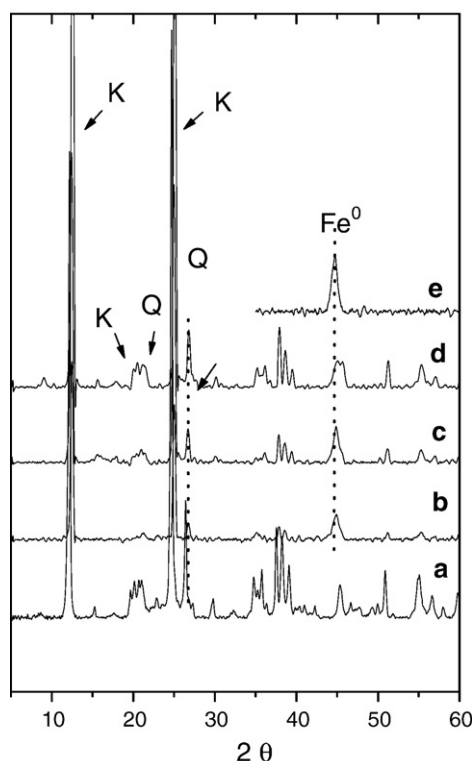
Fig. 1. XRD patterns of: (a) kaolinite; (b) nZVI-kaol1; (c) nZVI-kaol2; (d) nZVI-kaol5, and (e) pure nZVI. K: kaolinite, Q: quartz.

variety of reaction conditions; time, concentration, volume of solution/ mass of adsorbent (V/M) ratio, pH, and repetitive loading. Finally, the uptake mechanisms of both cations were discussed. The aqueous concentrations of Co and Cu were determined using Flame Atomic Absorption Spectroscopy (FAAS). The nZVI-kaol samples were characterized using Transmission Electron Microscopy (TEM), Selected Area Electron Diffraction (SAED), Scanning Electron Microscopy/ Energy-Dispersive X-ray Analysis (SEM/EDX), X-ray Photoelectron Spectroscopy (XPS) and powder X-ray Diffraction (XRD).

2. Experimental

2.1. Preparation of kaolinite-supported nZVI (nZVI-kaol)

Kaolinite used in this study was obtained from Fluka (03584). The characteristics of the kaolinite are provided in Section 3.1. The synthesis of nZVI-kaol was based on the borohydride reduction method, originally reported for synthesizing nZVI from Fe^{2+} ions (Wang and Zhang, 1997; Wang et al., 2006). In the relevant experiments, $FeCl_2 \cdot 4H_2O$ and $NaBH_4$ were used as iron and borohydride sources. The nZVI-kaol materials were synthesized such that the Fe:kaolinite mass ratio was 1:1, 0.5:1, or 0.2:1. For the 1:1 sample; 5.34 g $FeCl_2 \cdot 4H_2O$ was dissolved in a 4/1 (v/v) ethanol/water mixture (24 mL ethanol+6 mL deionized water), then 1.5 g kaolinite was added to this solution and the mixture was left in an ultrasonic shaker for 30 min in order to disperse the kaolinite grains. Meanwhile, 1.0 M sodium borohydride solution was prepared by dissolving 3.05 g $NaBH_4$ in 100 mL of deionized water. This offered a total BH_4^-/Fe^{2+} ratio of 3, providing excess borohydride to ensure the reduction of Fe^{2+} ions.

The borohydride solution was then added drop wise to the aqueous Fe^{2+}–kaolinite mixture while stirring continuously on a magnetic stirrer.
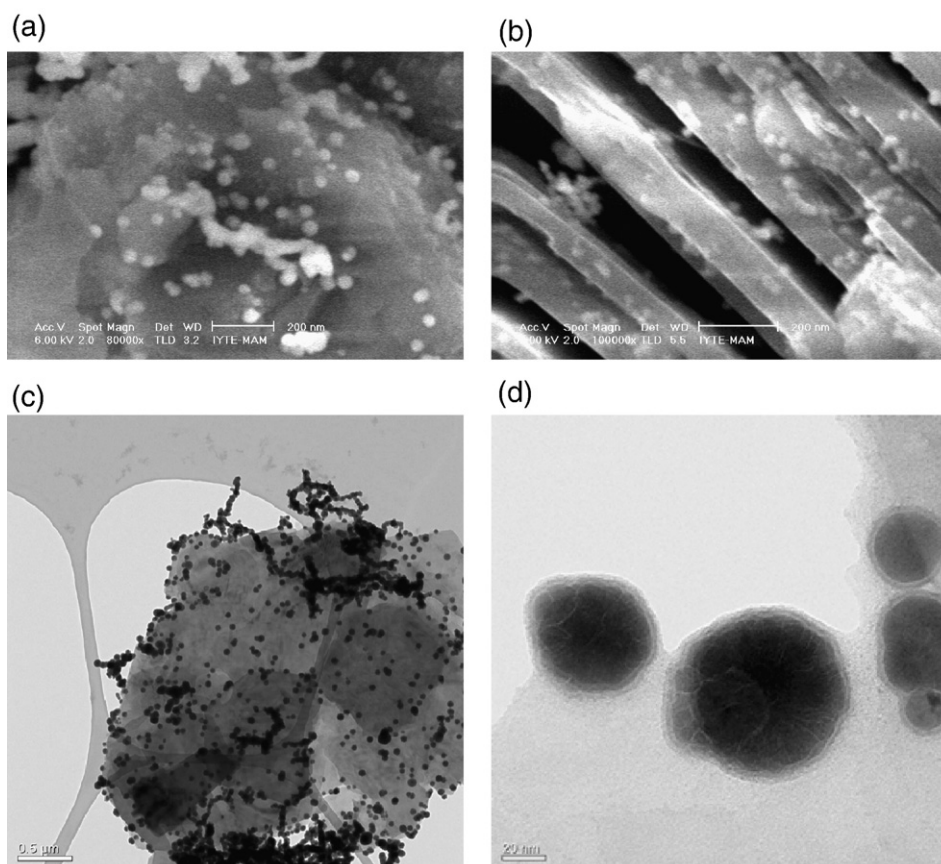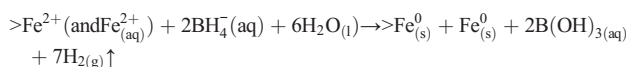

Fig. 2. (a,b) SEM images showing nZVI on the surface and edge sides of kaolinite, (c,d) typical TEM images of nZVI on kaolinite.

Black solid particles of nZVI appeared immediately following the addition of the first drop of NaBH$_4$ solution. After the full addition of the borohydride solution, the mixture was left for a further 10 min of stirring. The reduction of iron ions by borohydride ions can be represented by the reaction:

$$>Fe^{2+}(and Fe^{2+}_{(aq)}) + 2BH^-_4(aq) + 6H_2O_{(l)} \rightarrow >Fe^0_{(s)} + Fe^0_{(s)} + 2B(OH)_{3(aq)} + 7H_{2(g)}\uparrow$$

In the reaction, $>Fe^{2+}$ denotes iron ions attached to a kaolinite surface, $>Fe^0_{(s)}$ refers to nZVI dispersed on kaolinite, and $Fe^0_{(s)}$ stands for nZVI retaining its chain-like structure. Vacuum filtration was used to separate the solid from the liquid phase by multiple blue band Whatman filter papers. At this stage, the solid particles were washed at least three times with 25 mL portions of absolute ethanol. Finally, the synthesized material was oven-dried at 50 °C overnight. The samples with Fe:kaolinite ratios of 0.5:1 and 0.2:1 were synthesized following the same procedure except that the amounts of iron and borohydride ions were accordingly decreased. Throughout this text, the samples synthesized with Fe:kaolinite ratio of 1:1 are termed nZVI-kaol1; those synthesized at 0.5:1 ratio are termed nZVI-kaol2; and the samples synthesized at 0.2:1 ratio are named nZVI-kaol5.

The surface area of the nZVI-kaol samples was determined by the BET-N$_2$ method using a Micromeritics Gemini 5 instrument. The samples were degassed for 3 h at 353 K. In order to identify the iso-electric-point (IEP) of nZVI-kaol samples, the zeta potential was measured for a series of suspensions in the pH range 6.0–12.0. The measurements were conducted at a concentration of 0.1 g/L using a Zeta-Meter 3.0 instrument.

The particle size analysis of kaolinite was done using a Malvern Mastersizer 2000 instrument. For this purpose, 2.5 g of kaolinite was dissolved in 25 mL of Millipore water (18.2 MΩ) and the mixture was introduced to the instrument in small portions. More water was added to the suspension during analysis to increase the signal intensity, while subjecting the mixtures to ultrasonic shaking.

TEM and SAED characterization were performed using a Tecnai F20 instrument from FEI, operated at 200 kV acceleration voltage. Prior to analysis, the sample was dispersed in ethanol using an ultrasonic bath. Subsequently, a drop of the dispersion was applied to a holey carbon TEM support grid; excess solution was blotted off by a filter paper.

For XPS analysis, the samples were mounted in Al holders and analyzed under high vacuum ($<1\times10^{-7}$ mbar) in a Thermo Fisher Scientific Escascope X-ray photoelectron spectrometer. Al–K$_\alpha$ radiation (1486.6 eV) was used for the analysis. High-resolution scans were acquired with a 30 eV pass energy and 200 ms dwell times while
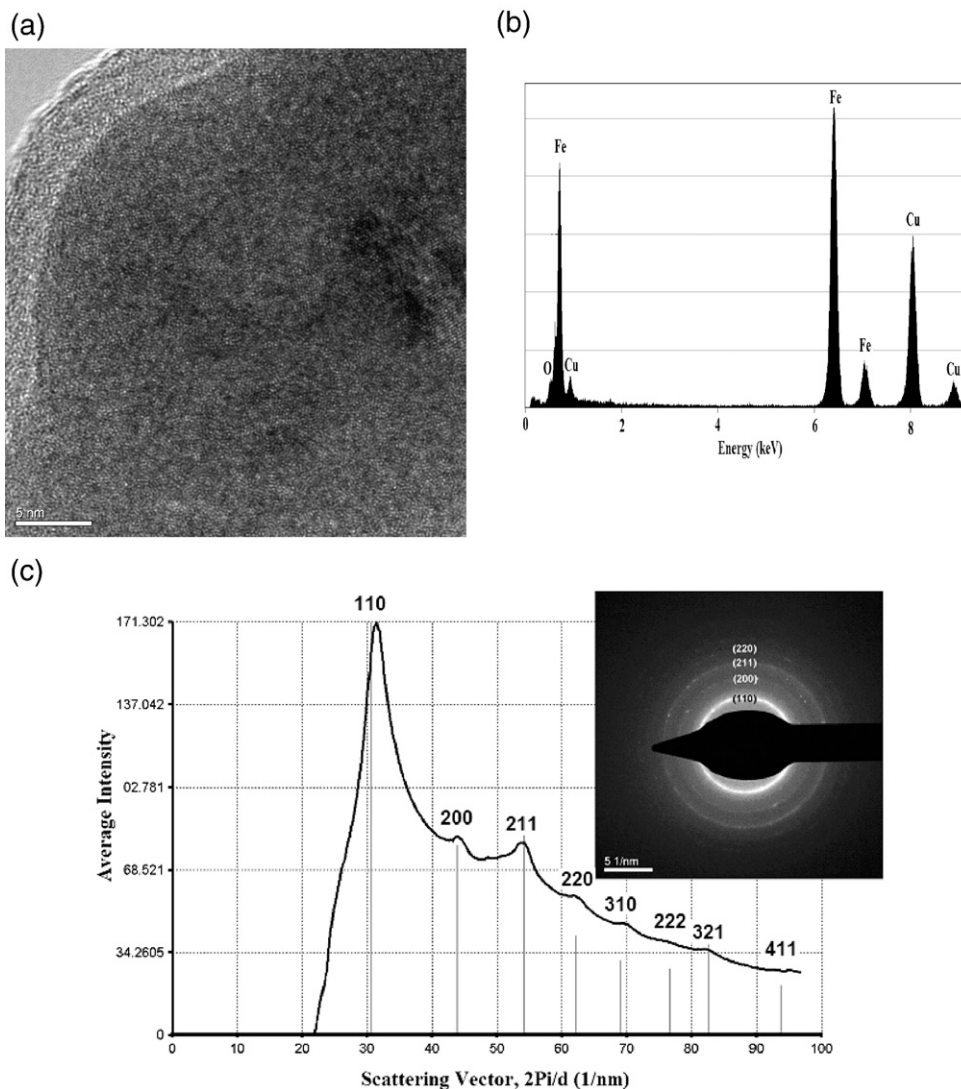

Fig. 3. (a) HR-TEM image showing the core-shell structure of an iron nanoparticle on kaolinite surface, (b) an EDX spectrum obtained from the core of an iron nanoparticle, (c) a polycrystalline SAED obtained from an area containing many iron nanoparticles.
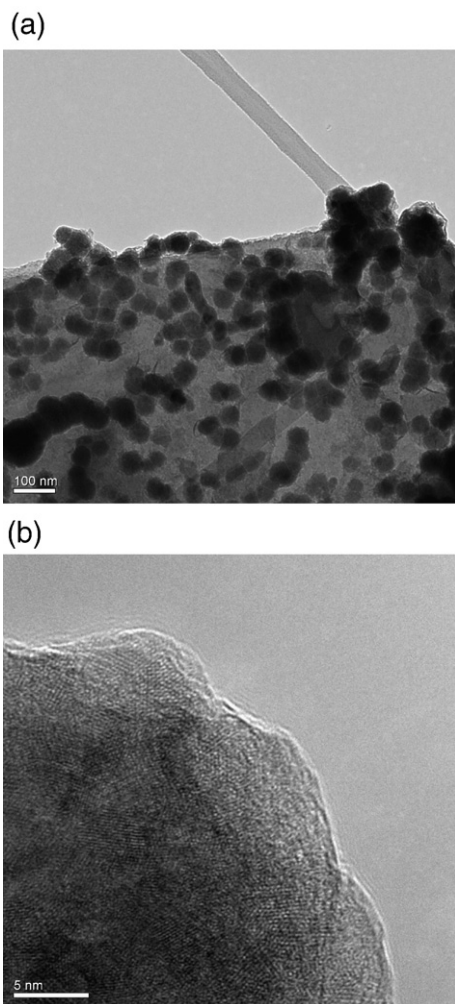
Fig. 4. HR-TEM images obtained for nZVI-kaol sample aged for 8 months at two different magnifications.

survey spectra were acquired with 100 eV pass energy and 200 ms dwell time. Data analysis was carried out using Pisces software.

XRD analysis was undertaken using a Philips X'Pert Pro instrument and Cu–K$_\alpha$ radiation ($\lambda = 1.54$ Å). Each sample was scanned within the 2θ range of 15–90°. SEM/EDX analysis was performed using a Philips XL-30S FEG instrument. The solid samples were first sprinkled onto adhesive carbon tapes supported on metallic disks. Secondary electron images of the sample surfaces were then recorded at different magnifications. Elemental and mapping EDX analysis was performed at randomly selected areas on the solid surfaces to elucidate the atomic distribution on the surface of the adsorbent material.

2.2. Uptake experiments

Throughout this study, Co^{2+} and Cu^{2+} solutions were prepared by dissolving 1.010 g of $CoCl_2 \cdot 6H_2O$ or 0.915 g of $Cu(NO_3)_2 \cdot ^5/_2H_2O$ in 250 mL of Millipore deionized water (18.2 MΩ) in a volumetric flask to yield 1000.0 mg/L stock solutions. These solutions were then used in preparing other solutions with lower concentrations by serial dilution. The experiments were carried out at ambient temperature and pressure using 50.0 mL falcon tubes. The tubes were kept on an orbital shaker operated at 350 rpm, and were later centrifuged at 6000 rpm. The supernatant solutions were transferred into clean falcon tubes and analyzed for their elemental contents using AAS. This analysis was done using a Thermo Elemental SOLAAR M6 Series atomic absorption spectrometer with air-acetylene flame.

To determine the effect of contact time on the extent of uptake of both metals, 0.050 g sample of nZVI-kaol1 or nZVI-kaol5 was added into 40.0 mL portions of 100.0 mg/L cation solutions (Co^{2+} or Cu^{2+}). The studied contact times were 1 min, 5 min, 10 min, 30 min, 1 h, 2 h, 4 h, 8 h, 16 h and 24 h.

In order to reveal the effect of initial metal ion concentration on the extent of uptake, 0.050 g of nZVI-kaol samples was added into 40.0 mL portions of metal solutions (Co^{2+} or Cu^{2+}) having initial concentrations of 1.0, 5.0, 10.0, 50.0, 100.0, 250.0 and 500.0 mg/L. The mixtures were shaken on the orbital shaker for 24 h and then removed for centrifugation. The experiments were performed using nZVI-kaol1 and nZVI-kaol5 samples. For the sake of comparison, parallel experiments were performed using kaolinite.

The effect of V/M ratio on the uptake of Co^{2+} or Cu^{2+} was studied by adding 0.050 g of nZVI-kaol5 into 10.0, 20.0, 30.0 and 40.0 mL portions of 50.0 mg/L or 500.0 mg/L metal solutions in 50 mL falcon tubes. The resulting V/M ratios were 200, 400, 600 and 800 mL/g, respectively. The tubes were shaken on an orbital shaker at 350 rpm for 24 h.

The effect of initial pH was studied at the values of 4.0, 6.0, 8.0 and 10.0. The initial pH was adjusted using 0.10 M aqueous solutions of HCl and NaOH. For this purpose, 0.050 g of nZVI-kaol5 was added into 40.0 mL portions of Co^{2+} or Cu^{2+} solution. The mixtures were shaken for 24 h and the pH of the solutions was measured at the end of shaking process.

To study the reusability of synthesized materials, a series of repetitive experiments was performed. In each experiment, 0.20 g of nZVI-kaol5 sample was added into 10.0 mL of 5.0 mg/L or 100.0 mg/L metal ion solution (Co^{2+} or Cu^{2+}) in a 50.0 mL falcon tube. After a shaking period of 45 min, the mixture was centrifuged, the supernatant solution was transferred into a clean tube, acidified and kept for AAS analysis. Successive trials were repeated eight times using each nZVI-kaol5 sample.

3. Results and discussion

3.1. Characterization of nZNI synthesized on kaolinite

Kaolinite samples used in this study included some quartz as the main impurity. The EDX analysis of kaolinite indicated that the average elemental atomic percentages are 66.8% O, 17.6% Si, 14.1% Al in addition to minor quantities of Na, K, Mg and Ca. The specific surface area of kaolinite was measured by BET-N$_2$ as 6.7 m^2/g. The diameter of the kaolinite particles, analyzed using a Malvern Mastersizer 2000 instrument, ranged between 0.4 and 52.5 μm, with more than 80% of these particles possessing a diameter varying between 1.1–17.4 μm.
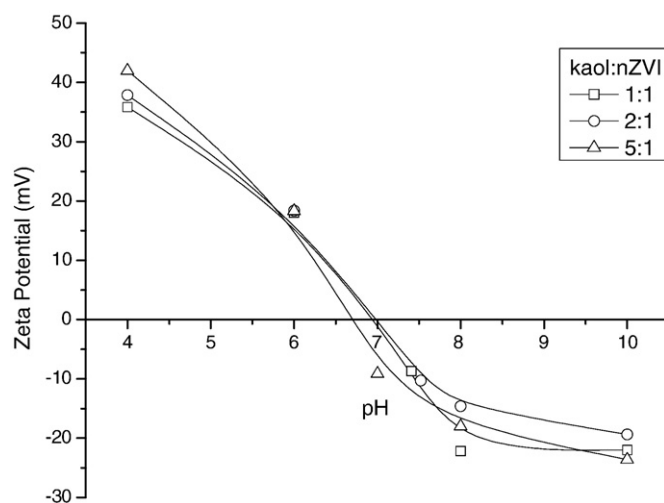

Fig. 5. Variation of the zeta potential with pH for nZVI-kaol samples. □: nZVI-kaol1, ○: nZVI-kaol2, △: nZVI-kaol5.

(a)

(b)

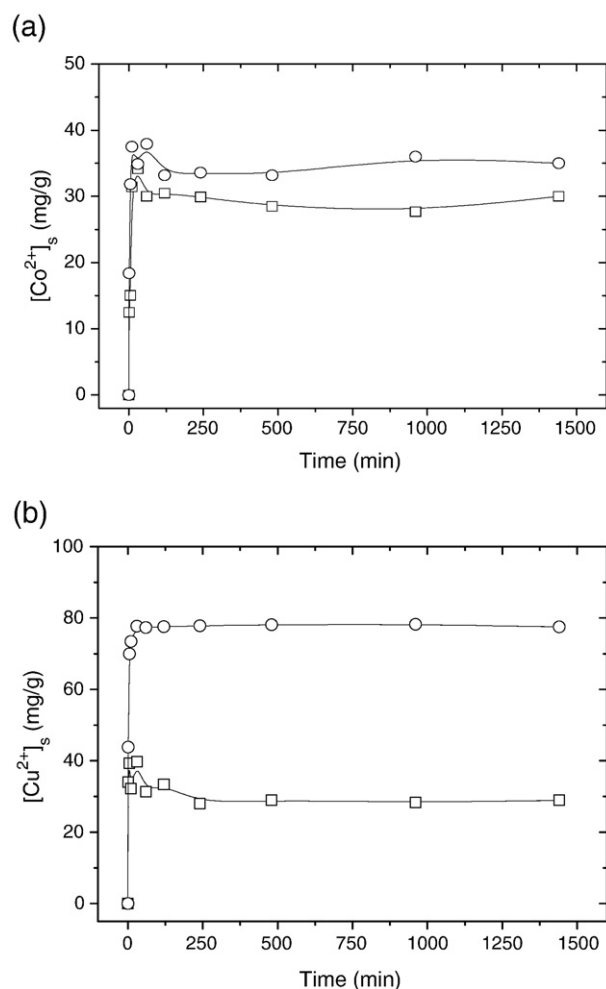**Fig. 6.** Variation of the adsorbed amount of: (a) Co^{2+}; or (b) Cu^{2+} as a function of time. ○: nZVI-kaol1, □: nZVI-kaol5.

(a)

(b)

Fig. 7. Variation of the equilibrium liquid concentration with concentration on the solid for: (a) Co^{2+}; or (b) Cu^{2+}. ○: nZVI-kaol1, □: nZVI-kaol5.

Typical XRD patterns of kaolinite in addition to freshly prepared nZVI-kaol samples are provided in Fig. 1. The formation of iron in its zero-valent (Fe^0) state is characterized by its major reflection at 2θ of 44.9°. Iron oxide signals were not detected in the XRD patterns of the freshly prepared samples.

The morphology and nanoparticle distribution of nZVI on kaolinite structure were analyzed using SEM and HR-TEM. Typical images of nZVI-kaol are shown in Fig. 2. SEM images (Fig. 2a,b) show the formation of dispersed iron nanoparticles on the surface and edges of kaolinite. In general, the edge sites of the clay mineral appeared to contain more nanoparticles in comparison to the surface sites. As indicated by TEM images (Fig. 2c,d), in addition to the dispersed nanoparticles, another portion of iron nanoparticles appears to persist with chain-like morphology that resembles that of pure nZVI. Qualitatively, the aggregated portion of nZVI seemed to decrease as the Fe^{2+} precursor concentration was lowered. The size of individual nZVI dispersed on kaolinite structure varied in the range 10–80 nm, and in general the size of dispersed nanoparticles seemed to decrease as the Fe^{2+} precursor concentration was decreased. In addition, some of the HR-TEM images showed that a small proportion of the iron nanoparticles were formed in between the layers of kaolnite leading to some minimal intercalation of iron nanoparticles into kaolinte.

Iron nanoparticles dispersed on kaolinite surface demonstrated the characteristic core-shell structure with the shell being about 2–3 nm thick, as shown by the HR-TEM image in Fig. 3a. Closer inspection of the obtained HR-TEM images showed an absence of any high resolution lattice fringes in the ima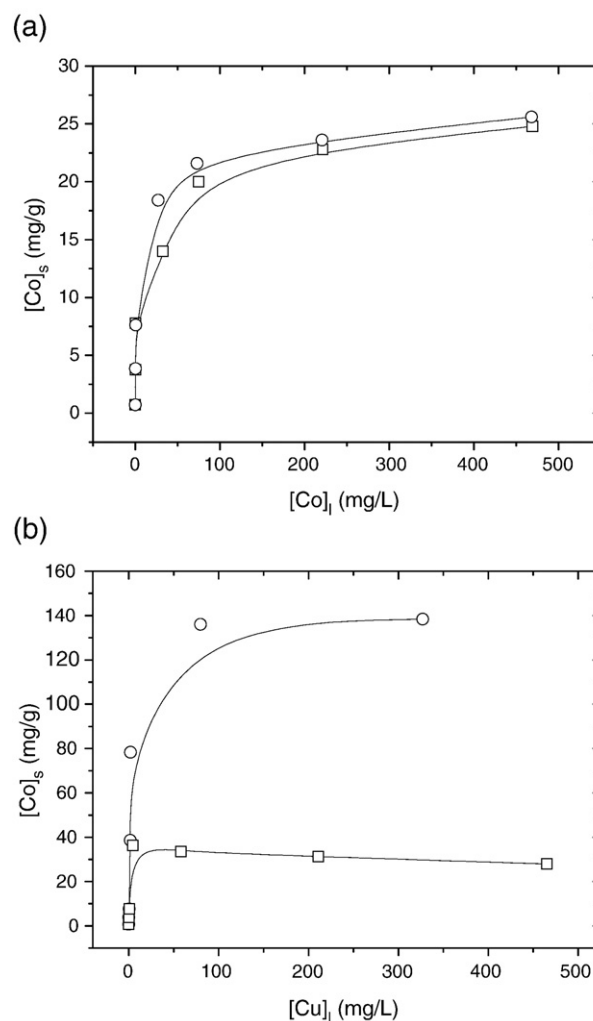ges of the shell structure, suggesting that the shell is of amorphous nature. The weak O signal in the EDX spectra recorded for iron nanoparticles confirmed that these nanoparticles are dominated by zero-valent iron, Fe^0 (Fig. 3b).

The crystal structure of Fe^0 was analyzed using Selected Area Electron Diffraction (SAED). A typical polycrystalline SAED pattern derived from many nanoparticles is presented as an inset in Fig. 3c. The pattern perfectly matches to a cubic structure with the space group Im–3m indicating that the core is ferromagnetic α-Fe (ICDD No 65-4899) with a lattice constant of a=2.867 Å. Moreover, there is no indication of any other crystal structure in the ED pattern, e.g. unidentified reflections, which corroborates that the iron oxide shell is of amorphous nature.

Table 1
% uptake of Co^{2+} and Cu^{2+} ions by nZVI-kaol5 at various V/M ratios, at initial metal concentrations of 50.0 and 500.0 mg/L

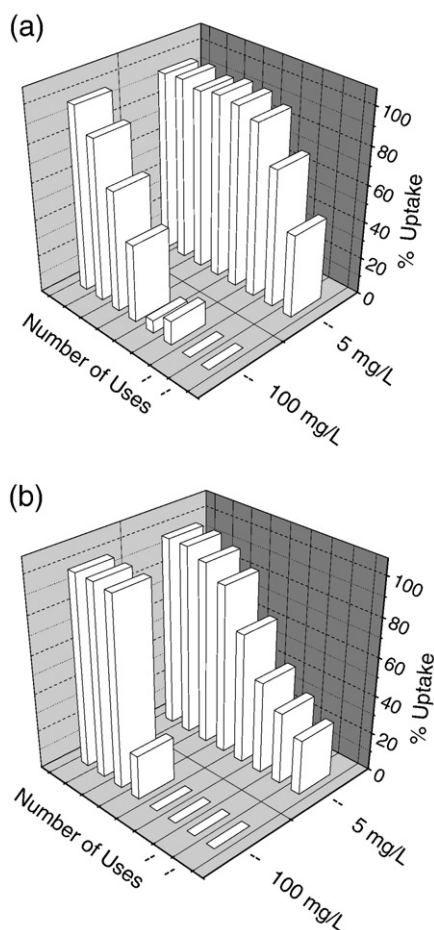| $[Me^{2+}]_0$ (mg/L)	M (g)	V (mL)	V/M (mL/g)	% Uptake of Co^{2+}	% Uptake of Cu^{2+}
50.0	0.050	40.0	800	52	64
	0.050	30.0	600	88	98
	0.050	20.0	400	97	98
	0.050	10.0	200	98	99
500.0	0.050	40.0	800	8	12
	0.050	30.0	600	9	17
	0.050	20.0	400	17	21
	0.050	10.0	200	28	49

(a)

(b)

Fig. 8. Variation of % uptake of: (a) Co^{2+}; and (b) Cu^{2+} with the number of successive uses of nZVI-kaol5.

The same analysis was also performed on nZVI-kaol samples aged for 8 months under normal conditions. HR-TEM images showed that iron nanoparticles largely retained their dispersion (Fig. 4a), and that the oxide-layer thickness did not exceed 5 nm (Fig. 4b).

The iso-electric points (IEPs) of nZVI-kaol samples prepared at different precursor concentrations were determined by measuring the zeta potentials at various pH values in the range 4.0–10.0. The results, given in Fig. 5, indicate that the IEPs occurred within the pH range of 6.7–7.0. For comparison, the IEP of pure nZVI was determined as 8.1, while that of kaolinite was 4.2. The given values of IEP for nZVI-kaol are, however, not representative for the whole adsorbent because nZVI was partially dispersed on kaolinite. None the less, in comparison to the IEP of pure nZVI, the determined IEPs for nZVI-kaol samples could offer an advantage for the removal of cations under environmental pH conditions.

The surface area of nZVI-kaol samples was determined by the BET-N_2 method. The BET and Langmuir surface areas for the nZVI-kaol1 material were 9.6 and 34.8 m^2/g, while those of the nZVI-kaol5 sample were 6.9 and 24.7 m^2/g, respectively.

Table 2
The equilibrium concentrations and % uptake corresponding to the uptake of 100.0 mg/L Co^{2+} and Cu^{2+} ions by nZVI-kaol5 at various initial pH values

pH	$[Co^{2+}]_l$ (mg/L)	$[Co^{2+}]_s$ (mg/g)	% Uptake	$[Cu^{2+}]_l$ (mg/L)	$[Cu^{2+}]_s$ (mg/g)	% Uptake
4.0	43	45	57	36	51	64
6.0	39	49	61	18	65	82
8.0	19	65	81	2	78	98
10.0	2	78	98	1	79	99

Fig. 9. XPS spectra showing the Fe 2p peaks in: (a) a reference Fe sample; (b) iron nanoparticles on kaolinite surface after Co^{2+} uptake; (c) iron nanoparticles on kaolinite surface after Cu^{2+} uptake.

3.2. Results of uptake experiments

The kinetic experiments were performed at mixing periods ranging from 5 min to 24 h. The results, given in Fig. 6, indicate that equilibrium

(a)

(b)

Fig. 10. XPS spectra showing: (a) Co 2p peaks; and (b) Cu 2p peaks obtained from kaolinite-nZVI samples after Co^{2+} and Cu^{2+} uptake. The initial concentration of the ions was 500 mg/L.

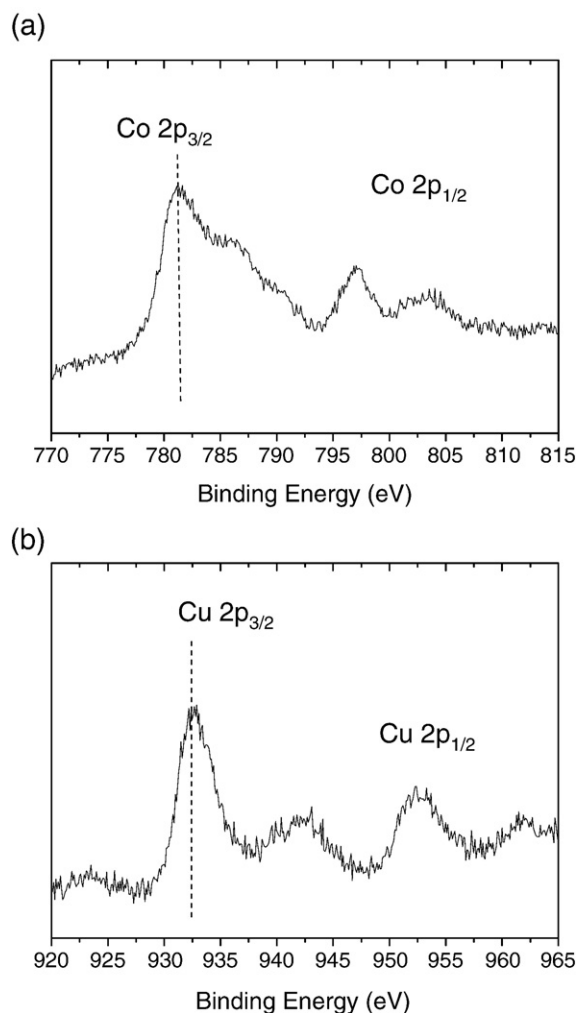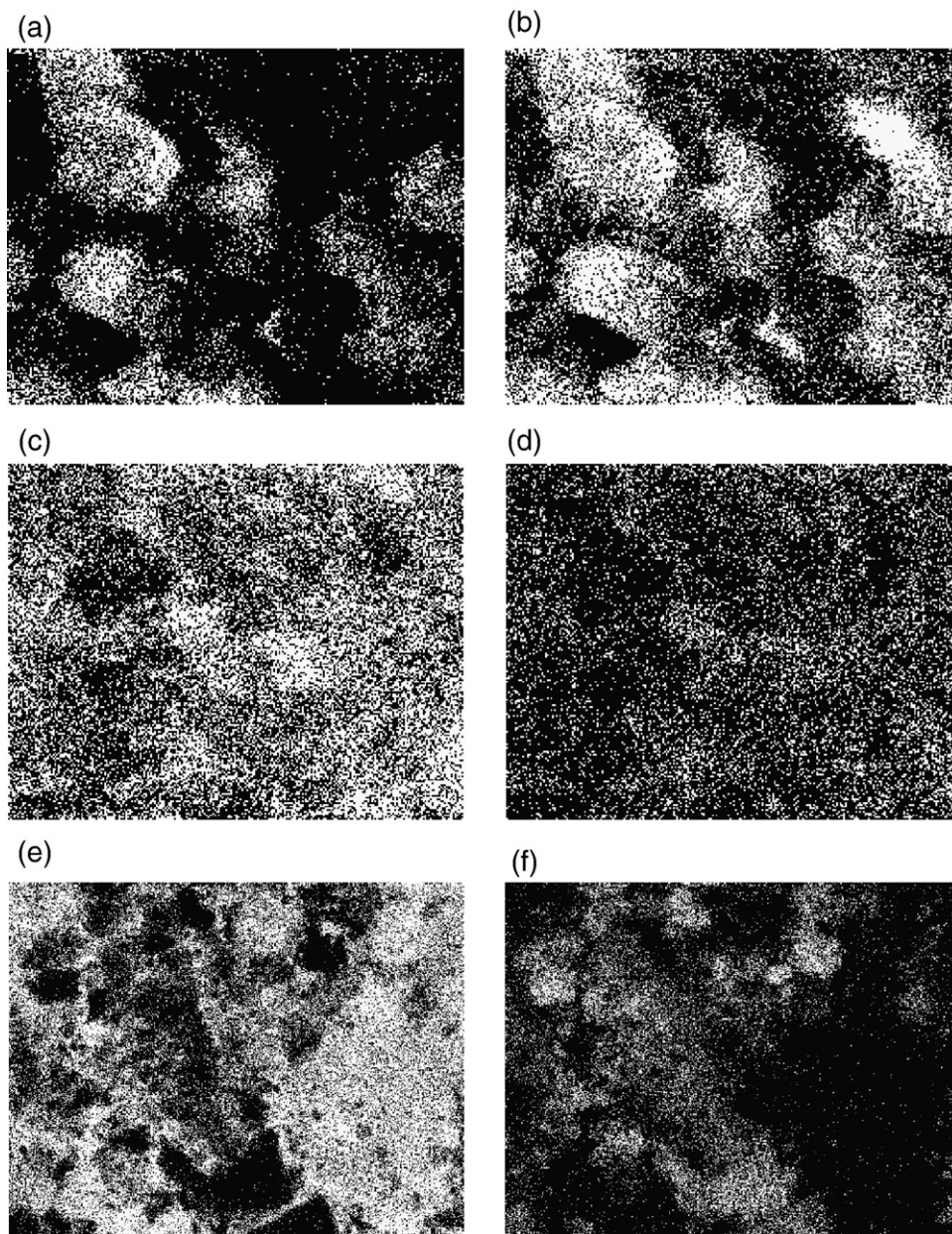**Fig. 11.** Elemental EDX mapping images of: (a) Al, (b) Si, (c) Fe, and (d) Co obtained from a nZVI-kaol sample loaded with 1000 mg/L Co^{2+} ions. The two EDX images in (e) and (f) show, respectively, the distribution of Fe and Cu obtained from an Fe-rich region on a nZVI-kaol sample loaded with 1000 mg/L Cu^{2+} ions.

is approached within the first 2–3 h of mixing for both nZVI-kaol1 and nZVI-kaol5 at the studied Co^{2+} and Cu^{2+} concentration of 100.0 mg/L.

The effect of initial concentrations was investigated in the range 1.0–500.0 mg/L while the V/M ratio was fixed at 800 mL/g (0.050 g adsorbent in 40.0 mL solution). The obtained isotherms are presented in Fig. 7. Both types of nZVI-kaol (nZVI-kaol1 and nZVI-kaol5) were more effective in the removal of Cu^{2+} compared to Co^{2+}. As estimated from the isotherms, the removal capacity of nZVI-kaol1 was around 25 mg/g for Co^{2+} and 140 mg/g for Cu^{2+}. When nZVI-kaol5 was applied, the removal capacity was around 23 mg/g for Co^{2+} and 32 mg/g for Cu^{2+}. The results suggest a strong correlation between the fixed amount of Cu^{2+} and the amount of nZVI in the adsorbent, while the uptake capacity of Co^{2+} decreased only slightly. These observations are discussed in relation with the fixation mechanisms of both cations in the next section.

In the uptake experiments in which nZVI-kaol5 is applied, the capacity of removal can be enhanced by increasing the amount of the adsorbent or reducing the volume of the solution — i.e. decreasing the V/M ratio. A set of experiments was performed to evaluate the change in the extent of uptake with the applied V/M ratio at the two initial concentrations of Co^{2+} and Cu^{2+} ions; 50.0 and 500.0 mg/L. The obtained results, summarized in Table 1, suggest that decreasing the V/M ratio leads to an almost complete removal of metal ions at the initial concentration of 50.0 mg/L, and increases the % uptake by up to four times at an initial metal ion concentration as high as 500.0 mg/L.

Since Fe-based materials are susceptible to oxidation in a wet environment, other sets of experiments were conducted to evaluate the effect of repetitive application on the removal capability of nZVI-kaol. These experiments were carried out at 5.0 and 100.0 mg/L initial concentrations of Co^{2+} and Cu^{2+} using nZVI-kaol5 as adsorbent. The results are drawn in Fig. 8 in term of uptake percentages. The nZVI-kaol samples appeared to remove more than 90% of 5.0 mg/L Co^{2+} and Cu^{2+} ions for 4–5 successive uses. When the metal concentration is increased to 100.0 mg/L, a fast deterioration in the reactivity of the adsorbent is seen to take place following the first application.

The solution pH is among the most critical factors that affect both the speciation of metal ion in solution, and the speciation of the surface of adsorbent in contact with the solution. A theoretical speciation analysis for cobalt and copper ions in solution was performed over a wide pH range using Visual MINTEQ software under various input conditions of temperature, ionic strength, and concentration. The results of cobalt analysis showed that up to pH values around 8, the dominant chemical form of Co in aqueous media was Co^{2+}. Beyond pH 9.0, $CoOH^+$ and $Co(OH)_2(aq)$ became increasingly prominent. The analysis of copper indicated that Cu^{2+} is the dominating chemical form up to pH of 7. With the increase in pH, forms such as $Cu(OH)^+$, $Cu_2(OH)_2^{2+}$, $Cu_3(OH)_4^{2+}$, $Cu(OH)_3^-$, and $Cu(OH)_2$ were predicted to prevail.

The results of the experiments that investigated the effect of initial pH on the extent of uptake are given in Table 2. The values show that the removal percentages of both Co^{2+} and Cu^{2+} ions increased with the increase in initial pH of the metal solutions. As noted previously in this text, the IEP of nZVI-kaol samples was in the pH range 6.7–7.0. The adsorption properties of oxide and oxyhydroxide groups on the shell of iron nanoparticles are strongly affected by the solution pH. It is reasonable to assume that the adsorption and surface coordination properties of iron nanoparticles are similar to those of classical metal oxides/hydroxides (Li and Zhang, 2007). When the solution pH exceeds the IEP, the oxide surface becomes negatively charged and consequently surface complexation reactions would be enhanced. At high cation concentrations, the electrostatic forces might also make a contribution to the fixation process. Under such conditions, the pH will be important in determining the thickness of the double layer at the interface between the oxide surface and solution. If the pH is below the IEP, the double layer becomes thicker due to repulsive forces between the positively charged surface and the cations, thus decreasing the chance for interaction between the adsorbate and the surface. As the pH increases beyond the IEP, the attractive forces between the negative charge on the surface and the adsorbate cations cause the double layer to shrink leading to a higher chance of adsorbate–surface interaction. In line with the trend observed throughout this study, higher removal percentages were observed for Cu^{2+} compared to Co^{2+} at all initial solution pH values.

In order to assess the uptake capacity of kaolinite, a separate set of experiments was performed using this clay mineral under conditions identical to those used to study the effect of concentration on nZVI-kaol. Within the studied range of concentrations, the uptake capacities of kaolinite toward Co^{2+} and Cu^{2+} ions did not exceed 5 and 8 mg/g, respectively, It was concluded that the nZVI component plays the major role in the fixation of both cations by the composite adsorbent. This was also confirmed by the EDX mapping analysis presented in the next section.

3.3. Mechanisms of uptake

The core-shell structure of iron nanoparticles enables them to demonstrate basically two uptake mechanisms toward metallic ions. The core, constituted of zero-valent iron, forms an electron source that might reduce ions possessing higher standard reduction potentials than iron. The shell, on the other hand, possesses hydroxyl groups at the interface with the solution and is capable as a result to fix adsorbate ions by surface complexation.

In this study, XPS analysis was conducted to reveal the oxidation states of cobalt and copper fixed by iron nanoparticles on the surface of nZVI-kaol samples. In addition, the chemical forms of Fe and O were analyzed to characterize the iron nanoparticles following the uptake process. The ability to distinguish between different oxidation states is one of the major strengths of the XPS technique. The related characterization is based on the binding energy shifts demonstrated by the photoelectrons when their atoms experience different chemical environments. Atoms of a higher positive oxidation state tend to exhibit higher binding energies due to the extra coulombic interaction

between the photoelectron and the ion core. The obtained results for nZVI-kaol samples loaded with Co^{2+} and Cu^{2+} ions are discussed below separately.

3.3.1. Co-Loaded nZVI-Kaol

An XPS spectrum that shows the Fe 2p photoelectron profile in a nZVI-kaol sample after being exposed to Co^{2+} ions at 500.0 mg/L concentration is shown in Fig. 9 (curve b). The XPS results indicate that iron nanoparticles on the kaolinite surface had undergone wet oxidation to form iron oxide/hydroxide species following the uptake of Co^{2+} ions. The Fe $2p_{3/2}$ line is centered at 711.7±0.1 eV binding energy. A similar value was previously reported for Fe in iron oxyhydroxide (FeOOH) (Wagner et al., 1979). The O 1s peak in the spectra is centered at 531.5 eV and displays strong asymmetry to the low binding energy side. In previous studies, O 1s in kaolinite was reported to occur at 531.3 eV (Lombardi et al., 2006). On the other hand, O 1s peak originating from O^{2-} in α-Fe_2O_3 (hematite) and that in γ-Fe_2O_3 (magheamite) were reported to occur at 530.0 eV and 529.9 eV, respectively. The same study reported also that O 1s peak arising from O^{2-} in the hydroxyl groups of α-FeOOH (goethite) and γ-FeOOH (lepidocrocite) occurred at 531.0 eV and 531.1 eV, respectively (Grosvenor et al., 2004). Curve fitting of the O 1s profile in our samples indicated signal contributions from O^{2-} in metal oxides (530.0 eV), and also from a more dominant peak at 531.5 eV, arising from a combination of signals from oxygen present in the kaolinite structure and in hydroxide phases e.g. FeOOH and/or $Co(OH)_2$. The oxide-related peak is estimated to account for ~36% of the recorded signal.

The recorded Co $2p_{3/2}$ peaks in the current study, shown in Fig. 10a, were located at 781.2±0.1 eV and were asymmetric to the high binding energy side. This value, which is identical to the one we reported earlier for Co-loaded nZVI (Üzüm et al., in press), occurs well above that reported in the literature for metallic cobalt, Co^0, i.e. 778.0±0.2 eV (Wagner et al., 1979; McIntyre and Cook, 1975), and is close to those reported earlier for Co^{2+} in cobalt oxide (780.0±0.2 eV) (McIntyre and Cook, 1975; McIntyre et al., 1990), and cobalt hydroxide (782.0±0.1 eV) (Tan et al., 1991).

Although Co^{2+} possesses a standard reduction potential (=−0.28 V at 298 K) that is somewhat larger than that of Fe^{2+} (=−0.44 V at 298 K), the reduction of Co^{2+} by Fe^0 might not take place. It is proposed that electron transfer from Fe^0 to the incoming cation, when equilibrium is established, might take place mainly via defects in the oxide shell (direct transfer), or through the conduction band of the oxide shell (indirect transfer) (Li and Zhang, 2007). For such a transfer to be thermodynamically favorable, the energy of the electrons in the iron metal and/or the oxide layer must be more negative than the standard potential of the redox couple of the incoming cation (Li and Zhang, 2007). As a result, unless direct electron transfer is taking place (the extent of which is unclear), the redox process will be governed by the Fermi energy (E_F) of the oxide shell, the value of which is reported to vary between −0.18 and −0.33 V (Balko and Tratnyek, 1998). With the standard potential of the Co^{2+}/Co^0 redox couple in mind (=−0.28 V at 298 K), an effective overlap between the unoccupied electron energy levels of the incoming Co^{2+} and the conduction band of the oxide shell to produce Co^0 seems to be doubtful. This approach assumes that the given values for bulk iron are not very different from those of iron nanoparticles and as such should be viewed as a first approximation that requires further electrochemical consideration.

Based on the above, it is most likely that the uptake mechanism of Co^{2+} on nZVI-kaol involves chemical complexation to the exposed hydroxyl groups in addition to precipitation at high metal ion concentrations.

3.3.2. Cu-Loaded nZVI-kaol

The recorded Fe 2p photoelectron profile from Cu-loaded nZVI-kaol is shown in Fig. 9c. The Fe $2p_{3/2}$ line was centered at 711±0.1 eV. Unlike Fe $2p_{3/2}$ peak in Co-loaded nZVI-kaol sample, this binding energy value is very close to that reported previously (Grosvenor et al., 2004) for Fe in γ-Fe_2O_3 (711.0 eV) and is well below those reported for

Fe in α-FeOOH (711.4 eV) and γ-FeOOH (711.5 eV). However, the O 1s was centered at 531.5 eV and displayed strong asymmetry to the low binding energy side, similar to that reported in the previous section.

The Cu $2p_{3/2}$ lines in the Cu-loaded nZVI-kaol were centered at a binding energy of 932.3 ± 0.1 eV, as shown in Fig. 10b. Our measurement of the same peak for Cu-loaded pure nZVI coincides with this observation. The given value is very close to the Cu $2p_{3/2}$ lines previously reported for Cu^0 (932.6 ± 0.2 eV) (Wagner et al., 1979), and Cu^+ in Cu_2O (932.4 ± 0.3 eV) (Wagner, 1975). The Auger parameter, a powerful tool for elucidating the electronic environment of an atom in various compounds, was calculated in order to distinguish between the two oxidation states of Cu. This parameter is defined as the sum of the relevant Cu $2p_{3/2}$ core ionization photoelectron energy, E_B, and the appropriate Auger electron kinetic energy, E_K for the same element of interest. In this case, the Auger line of interest is Cu LMM occurring at 570.2 eV. Based on the measured values of E_B (932.3 eV) and E_K (1486.6–570.2 eV), the copper Auger parameter was here calculated as 1848.7 eV, indicating that the recorded signal was derived from Cu^+ rather than Cu^0. This result shows that Cu^{2+} ions are reduced by Fe^0 primarily to Cu^+ (in the form of Cu_2O). Moreover, the recorded Cu 2p lines were asymmetric to the high binding energy side, indicating that complete Cu reduction had not occurred, and that some small portion remained in a Cu^{2+} oxidation state.

The oxidation–reduction mechanism associated with the uptake of Cu^{2+} ions by iron nanoparticles is justified by the fact that the standard potentials of the Cu^{2+}/Cu^0 (= +0.34 V at 298 K) and Cu^{2+}/Cu^+ (= +0.16 V at 298 K) couples are both well above that of Fe^{2+}/Fe^0 (= −0.44 V at 298 K). As a result, the energy of the electrons in the conduction bands of iron metal and/or iron oxide will be distinctly more negative than the standard potential of both reduction couples, creating an effective driving force for electron transfer from zero-valent iron to the fixed Cu^{2+} ions.

As the uptake experiments presented earlier in this text have shown, under equivalent experimental conditions, the extent of removal of Cu^{2+} ions is greater than that of Co^{2+} ions. The uptake trend seems to be closely related to the mechanism of removal, with the redox route observed in the Cu^{2+} case leading to greater removal than the adsorption mechanism operating with Co^{2+} case. As given in Section 3.2, the uptake capacity of nZVI-kaol1 towards Cu^{2+} was around 140 mg/g, while that of Co^{2+} was 25 mg/g. When the amount of iron precursor is decreased to one-fifth of its initial amount, as is the case in the nZVI-kaol5 composite, the removal capacity of Cu^{2+} goes down to 32 mg/g, probably as a result of decrease in the amount of electron source (nZVI) in the adsorbent. In the case of Co^{2+}, apparently fixed by a adsorption mechanism, the uptake capacity decreases slightly to about 23 mg/g upon applying nZVI-kaol5 as the adsorbent. Since the extent of adsorption is dependent on the availability of surface sites, the observed result seems to originate from the enhancement in the dispersion of nZVI on the kaolinite surface as a result of decreasing the amount of Fe precursor during synthesis of nZVI-kaol5.

The results of the XPS surveys conducted in this study for Co^{2+} and Cu^{2+} uptake on nZVI-kaol coincide with those reported recently for the uptake of each of the two ions on pure nZVI (Üzüm et al., in press; Karabelli et al., 2008). Hence, although preparing nZVI in the presence of kaolinite affects the extent of aggregation of the nanoparticles, the mechanism of interaction between the adsorbate cations and iron nanoparticles seems to be unaffected.

Energy-Dispersive X-ray (EDX) mapping analysis was used to reveal the distribution of Co and Cu signals on the surface of nZVI-kaol samples after loading them with 1000.0 mg/L initial concentrations of Co^{2+} and Cu^{2+} ions. Typical elemental maps are shown in Fig. 11. The distributions of Al and Si elements (Fig. 11a,b), which form the backbone of the clay mineral are observed to coincide except for some Si-rich regions which possibly originate from minor amounts of associated quartz. The signals of Co and Cu showed weak correlation

with those of Al and Si, indicating that kaolinite fraction in the nZVI-kaol adsorbent was not favored during adsorption. On the other hand, Co signals seem to be strongly associated with those of Fe, suggesting selective binding to the nZVI component of the adsorbent (Fig. 11c,d). Here it must be noted that possible overlap might take place between the EDX lines of Co K_α with Fe K_β, due to their close energies, In the case of Cu, the X-ray maps recorded in Fe-rich regions in the adsorbent reveal the formation of intense and distinct domains that do not correlate also with Fe signals in nZVI-kaol (Fig. 11e,f). Taking also into consideration the XPS findings, these domains can be attributed to Cu_2O and Cu^0 phases, a result that agrees with that we reported recently for Cu^{2+} uptake by pure nZVI (Karabelli et al., 2008).

4. Conclusions

The presence of kaolinite during the synthesis of iron nanoparticles leads to a partial decrease in their extent of aggregation, producing dispersed nanoparticles with sizes varying between 10 and 80 nm. When the Fe^{2+} precursor concentration was decreased, better dispersion was qualitatively observed. The dispersed ZVI nanoparticles showed the characteristic core-shell structure.

Kaolinite-supported nZVI (nZVI-kaol) demonstrated higher uptake capacities toward Cu^{2+} ions compared to Co^{2+} ions. According to XPS results, Co^{2+} ions were fixed through adsorption and precipitation mechanisms, while Cu^{2+} ions were fixed mainly through a redox mechanism that lead to the formation of Cu_2O and to a lesser extent Cu^0.

More effort is still needed to achieve better dispersion of nZVI on kaolinite surfaces, the thing that necessitates further manipulations of the starting kaolinite to iron ratios.

References

Baird, C., 1999. Environmental Chemistry. W.H. Freeman, New York.
Balko, B.A., Tratnyek, P.G., 1998. Photoeffects on the reduction of carbon tetrachloride by zero-valent iron. J. Phys. Chem. B 102, 1459–1465.
Blowes, D.W., Ptacek, C.J., Benner, S.G., Mcrae, Che, W.T., Bennett, T.A., Puls, R.W., 2000. Treatment of inorganic contaminants using permeable reactive barriers. J. Contam. Hydrol. 45, 123–137.
Çelebi, O., Üzüm, Ç., Shahwan, T., Erten, H.N., 2007. A radiotracer study of the adsorption behavior of aqueous Ba^{2+} ions on nanoparticles of zero-valent iron. J. Hazard. Mater. 148, 671–676.
Grosvenor, A.P., Kobe, B.A., Biesinger, M.C., McIntyre, N.S., 2004. Investigation of multiplet splitting of Fe 2p Xps spectra and bonding in iron compounds. Surf. Interface Anal. 36, 1564–1574.
Huber, D.L., 2005. Synthesis, properties, and applications of iron nanoparticles. Small 1, 482–501.
Kanel, S.R., Manning, B., Charlet, L., Choi, H., 2005. Removal of arsenic(Iii) from groundwater by nanoscale zero-valent iron. Environ. Sci. Technol. 39, 1291–1298.
Kanel, S.R., Greneche, J.M., Choi, H., 2006. Arsenic(V) removal from groundwater using nano scale zero-valent iron as a colloidal reactive barrier material. Environ. Sci. Technol. 40, 2045–2050.
Karabelli, D., Uzum, C., Shahwan, T., Eroglu, A.E., Scott, T., Hallam, K.R., Lieberwirth, I., 2008. Batch removal of aqueous Cu^{2+} ions using nanoparticles of zero-valent iron: a study of the capacity and mechanism of uptake. Ind. Eng. Chem. Res. 47, 4758–4764.
Li, X.Q., Zhang, W.-X., 2006. Iron nanoparticles: the core-shell structure and unique properties for Ni(Ii) sequestration. Langmuir 22, 4638–4642.
Li, X.Q., Zhang, W.-X., 2007. Sequestration of metal cations with zerovalent iron nanoparticles — a study with high resolution X-Ray photoelectron spectroscopy (Hr-Xps). J. Phys. Chem. C 111, 6939–6946.
Li, L., Fan, M., Brown, R.C., Leeuwen, J.V., Wang, J., Wang, W., Song, Y., Zhang, P., 2006. Synthesis, properties, and environmental applications of nanoscale iron-based materials: a review. Crit. Rev. Environ. Sci. Technol. 36, 405–431.
Lombardi, K.C., Mangrich, A.S., Wypych, F., Rodrigues-Filho, U.P., Guimarães, J.L., Schreiner, W.H., 2006. Sequestered carbon on clay mineral probed by electron paramagnetic resonance and X-Ray photoelectron spectroscopy. J. Colloid Interface Sci. 295, 135–140.

Macdonald, J.E., Kelly, J.A., Veinot, J.G.C., 2007. Iron/iron oxide nanoparticle sequestration of catalytic metal impurities from aqueous media and organic reaction products. Langmuir 23, 9543–9545.

McIntyre, N.S., Cook, M.G., 1975. X-ray photoelectron studies on some oxides and hydroxides of cobalt, nickel, and copper. Anal. Chem. 47, 2208–2213.

McIntyre, N.S., Johnston, D.D., Coatsworth, L.L., Davidson, R.D., Brown, J.R., 1990. X-ray photoelectron spectroscopic studies of thin film oxides of cobalt and molybdenum. Surf. Interface Anal. 15, 265–272.

Ponder, S.M., Darab, J.G., Mallouk, T.E., 2000. Remediation of Cr(Vi) and Pb(Ii) aqueous solutions using nanoscale zero-valent iron. Environ. Sci. Technol. 34, 2564–2569.

Tan, B.J., Klabunde, K.J., Sherwood, P.M.A., 1991. Xps studies of solvated metal atom dispersed (Smad) catalysts; evidence for layered cobalt–manganese particles on alumina and silica. J. Am. Chem. Soc. 113, 855–861.

Tratnyek, P.G., Johnson, R.L., 2006. Nanotechnologies for environmental cleanup. Nano Today 1, 44–48.

Üzüm, Ç., Shahwan, T., Eroğlu, A.E., Lieberwirth, I., Scott, T.B., Hallam, K.R., in press. Application Of Zero-Valent Iron Nanoparticles For The Removal Of Aqueous Co^{2+} Ions Under Various Experimental Conditions. Chem. Eng. J.

Wagner, C.D., 1975. Chemical shifts of Auger lines, and the auger parameter. Faraday Discuss. Chem. Soc. 60, 291–300.

Wagner, C.D., Riggs, W.M., Davis, L.E., Moulder, J.F., Muilenberg, G.E., 1979. Handbook Of X-Ray Photoelectron Spectroscopy. Perkin-Elmer Corporation, Physical Electronics Division, Eden Prairie, Minn., p. 55344.

Wang, C., Zhang, W., 1997. Synthesizing nanoscale iron particles for rapid and complete dechlorination of TCE and PCBS. Environ. Sci. Technol. 31, 2154–2156.

Wang, W., Jin, Z., Li, T., Zhang, H., Gao, S., 2006. Preparation of spherical iron nanoclusters in ethanol–water solution for nitrate removal. Chemosphere 65, 1396–1404.

Zhang, W.X., 2003. Nanoscale iron particles for environmental remediation: an overview. J. Nanopart. Res. 5, 323–332.

Zhang, H., Jin, Z.H., Han, L., Qin, C.H., 2006. Synthesis of nanoscale zero-valent iron supported on exfoliated graphite for removal of nitrate. Trans. Nonferr. Met. Soc. China 16, S345–S349.